Tuomi, Sami; Pakkanen, Olli J.; Borghei, Maryam; Kronberg, Rasmus; Sainio, Jani; Kauppinen, Esko I.; Nasibulin, Albert G.; Laasonen, Kari; Kallio, Tanja

# Experimental and Computational Investigation of Hydrogen Evolution Reaction Mechanism on Nitrogen Functionalized Carbon Nanotubes

*Published in:*
ChemCatChem

*DOI:*
10.1002/cctc.201800479

Published: 07/09/2018

*Document Version*
Peer-reviewed accepted author manuscript, also known as Final accepted manuscript or Post-print

*Please cite the original version:*
Tuomi, S., Pakkanen, O. J., Borghei, M., Kronberg, R., Sainio, J., Kauppinen, E. I., Nasibulin, A. G., Laasonen, K., & Kallio, T. (2018). Experimental and Computational Investigation of Hydrogen Evolution Reaction Mechanism on Nitrogen Functionalized Carbon Nanotubes. *ChemCatChem*, *10*(17), 3872-3882. https://doi.org/10.1002/cctc.201800479

# Experimental and Computational Investigation of Hydrogen Evolution Reaction Mechanism on Nitrogen Functionalized Carbon Nanotubes

Sami Tuomi[a], Olli J. Pakkanen[b], Dr. Maryam Borghei[c],[d], Rasmus Kronberg[a], Dr. Jani Sainio[e], Prof. Esko I. Kauppinen[d], Prof. Albert G. Nasibulin[f],[d], Prof. Kari Laasonen[b], Prof. Tanja Kallio[a],[g] *

## Abstract

Designing earth-abundant element based efficient and durable electrocatalysts for hydrogen evolution reaction (HER) is attracting growing attention as the renewable electricity supply sector urgently needs sustainable methods for storing energy. Nitrogen functionalized carbon nanomaterials are an interesting electrocatalysts option because of their attractive electrical properties, excellent chemical stability and catalytic activity. Hence, this study reports the HER mechanism on nitrogen functionalized few-walled carbon nanotubes (N-FWCNT). With this earth-abundant element based catalyst 250 mV overpotential is required to reach 10 mA $cm^{-2}$ current density and so its HER activity is comparable to other non-noble metal catalysts, and clearly among the highest previously reported for N-FWCNTs. To gain fundament insight on their functioning, computational analysis has been carried out to verify the effect of nitrogen and to analyze the reaction mechanism. The reaction mechanism has also been analyzed experimentally

[a] *Research Group of Electrochemical Energy Conversion and Storage, Department of Chemistry and Material Science, Aalto University, P.O. Box 16100, 00076 Aalto, Finland*

[b] *Research Group of Computational Chemistry, Department of Chemistry and Material Science, Aalto University, P.O. Box 16100, 00076 Aalto, Finland*

[c] *Bio-based Colloids and Materials, Department of Bioproducts and Biosystems, Aalto University, P.O. Box 16300, 00076 Aalto, Finland*

[d] *Department of Applied Physics, School of Science, Aalto University, P.O. Box 15100, FI-00076 Aalto, Finland*

[e] *Surface Science Group, Department of Applied Physics, Aalto University, P.O. Box 15100, 00076 Aalto, Finland*

[f] *Skolkovo Institute of Science and Technology, 100 Novaya str., Skolkovo, Moscow Region, 143025, Russia*

[g] *National University of Science and Technology "MISiS" Department of Functional Nanosystems and High-Temperature Materials, 119049, Moscow, Leninsky Avenue, 4*

with a pH series, and both the methods suggest that the HER proceeds *via* the Volmer-Heyrovský mechanism. Overall hydrogen surface coverage on N-FWCNT is also suggested to affect the HER rate. Interestingly, in the studied structure, carbons in vicinity of nitrogen atoms, but not directly bound to nitrogen, appear to promote the HER most actively. Furthermore, durability of N-FWCNTs has been demonstrated by operating a full electrolyzer cell for five weeks.

## Keywords

Hydrogen reduction mechanism, hydrogen evolution catalysis, carbon nanotubes, nitrogen doping

## 1 Introduction

We are witnessing fast transition towards solar and wind based energy supply indicated by drastic increase of installed renewable energy supply capacity [1]. However, above-mentioned technologies are inherently intermittent energy sources and consequently, energy storage is becoming the bottleneck for this transition. Electrochemical conversion of the excess electric energy into chemical bond energy is one promising approach for energy storage as chemicals can couple the energy sector to transport and chemical industry sectors. In this regard, electrocatalysis of the hydrogen evolution reaction (HER) is widely studied as it is the cathode reaction in water electrolysis, which is considered as one of the key technologies for intermittent renewable energy conversion and storage. For this electrolysis process to proceed with appreciable rate, effective electrocatalysts are required to overcome the reaction barriers. Currently, platinum is the most widely used HER catalyst under acidic conditions in polymer electrolyte membrane electrolyzers, but the high price and scarcity of the material have driven scientists to develop novel high-performing non-precious metal alternatives. Development of new electrocatalysts, and optimizing their activity, requires fundamental understanding of the reaction sites, energy barriers and effect of reaction conditions. Therefore, it is important not only to measure catalytic activity of new potential catalyst materials but also to scavenge the origin of the catalytic properties.

Modified carbon nanomaterials, such as carbon-encapsulated metals and various doped carbon nanotube materials have shown great potential as Pt-replacing catalysts for the HER. [2-6] While pristine carbon nanotubes are poor electrocatalysts, they have appealing electrical and structural properties that form an excellent backbone for electrocatalyst development.

Recently, nitrogen doped carbon nanotubes have attracted a lot of attention due to their high electrocatalytic activity and stability for the oxygen reduction and evolution reactions in alkaline media [7-10]. Moreover, these catalysts consist only of earth-abundant elements, which is important regarding price and supply security of the raw materials. Hence, for the above-mentioned reaction, it can successfully replace Pt-based electrocatalysts. On the other hand, N-functionalized CNTs have recently shown to have activity also towards the HER both under acidic and alkaline media [11,12].

Previously, we have reported high ORR activity of N-doped few-walled carbon nanotubes (N-FWCNTs) with low nitrogen content (0.5 wt%) in alkaline media [13]. In that study, potential activity of N-FWCNTs toward the HER has been also observed. Herein this effort, more detailed investigation of the HER activity and mechanism is carried out by electrochemical experimental and computational methods. The catalysts have been prepared using our method for synthetizing highly active ORR catalysts [13] by in-situ polymerization of polyaniline (PANI) on functionalized high-quality FWCNTs, followed by pyrolysis. The performance of the electrocatalysts has been measured in various temperatures and electrolytes and Tafel slope analysis and pH variation are used to determine the reaction mechanism of the HER. The experimental results are complemented with computational study of the effect of two graphitic nitrogen atoms on the HER reaction steps. The reaction barriers are investigated using the charge neutral and charged CNTs, and the effect of hydrogen coverage is also included.

Based on the activity measurements, our material show higher HER activity than earlier reported for N-CNT [11] and comparable to those of the state-of-the-art non-noble metal catalysts. In addition, integration and long-term stability of the N-FWCNT catalyst has been verified in an electrolyzer cell, which is crucial for commercial applications. For the analysis of the reaction mechanism, both the experimental and computational approach shows the Volmer-Heyrovský reaction mechanism to be dominant at high proton surface coverages and high overpotential.

Moreover, hydrogen overpotential deposition appears to proceed the HER reaction. Interestingly, in the studied structure carbons in vicinity of nitrogen atoms, but not directly bound to nitrogen, appear to promote the HER most actively.

## 2 Experimental and procedures

### 2.1 Synthesis of the catalysts

N-FWCNTs were prepared with the methodology reported earlier [13]. Briefly, FWCNTs were synthesized *via* chemical vapor deposition (CVD) and purified with HCl to remove the metal residues. In order to produce oxygen functional groups on the nanotube walls, functionalization treatment was carried out on FWCNTs using 2 M $HNO_3$/1 M $H_2SO_4$ at 120 °C for 4, 6 and 8 hours. Then, PANI was deposited on the functionalized FWCNTs (mass ratio of 50 %) through in-situ oxidizing aniline monomer with ammonium persulfate (APS) in 1 M HCl. Finally, the PANI-FWCNT composites were subjected to pyrolysis at 900 °C for 2 h to obtain N-FWCNTs. The samples are denoted as N-FWCNT-4, N-FWCNT-6, N-FWCNT-8, for the samples treated for 4, 6 and 8 h of acid functionalization, respectively.

### 2.2 Characterization of the catalysts

X-ray photoelectron spectroscopy (XPS) was carried out with a Kratos Axis Ultra spectrometer using monochromated Al $K_\alpha$ radiation, a pass energy of 40 eV, an X-ray power of 150 W and an analysis area of roughly 700 µm x 300 µm. The nitrogen 1s spectrum was fitted with Gaussian peaks after a linear background subtraction. The positions of the peaks were fixed to within ± 0.1 eV of given biding energies and their full width at half maximum (FWHM) was confined to be equal, excluding the N-oxide peak, which covers several different species.

High resolution transmission electron microscopy (HR-TEM) was conducted with a JEOL double Cs-corrected TEM (JEM-2200FS) operated at an acceleration voltage of 200 kV.

Raman analysis was performed using a Horiba Lab RAM HR spectrometer equipped with a CCD camera and 633 nm excitation laser.

## 2.3 Electrochemical measurements

The electrocatalytic HER activities of the N-FWCNT catalysts were investigated with rotating disc electrode (RDE) experiments using glassy carbon (GC) electrode with a radius of 5 mm (*Pine Instruments*). Pristine FWCNTs and commercial 60 wt% Pt/C (*Sigma-Aldrich*) were used as reference materials. Catalyst inks were prepared by mixing the catalyst powder with 5 wt% Nafion (*Sigma-Aldrich*) and ethanol solution. Droplet of the ink was deposited on the electrode to yield a catalyst loading of approximately 0.55 $mg \cdot cm^{-2}$ and Nafion content of 0.43 $mg \cdot cm^{-2}$. The experiments were carried out in a 0.5 M $H_2SO_4$ solution with $N_2$ bubbling at ambient temperature with 10 mV $s^{-1}$ scan rate and 3000 rpm rotation. A nickel foam was used as a counter electrode and a reversible hydrogen electrode (RHE) as a reference electrode. The measurement equipment consisted of an Autolab PGSTAT100 potentiostat and a Pine Instruments MSR rotator. All the potentials are given against the RHE and currents are normalized against the geometrical area of the GC electrode. For logarithmic curves, background corrected currents are obtained by deducting the background current observed at 0 V vs. RHE to enable comparison between different batches with varying background currents. In effect, this action affects currents at potentials more positive than -0.2 V vs. RHE and this ranges has not been used for data analysis. Electrochemical impedance spectroscopy analysis was carried out from 10,000 Hz to 0.1 Hz with overpotentials of 0 and 200 mV using 5 mV amplitude. Electrolyzer cell experimental is presented in Supporting Information.

## 2.4 Computational details

Fully periodic spin-polarized density functional theory calculations were performed with the free CP2K software [14,15] employing the Quickstep module [16]. The exchange-correlation energy was approximated with the generalized gradient approximation (GGA) by Perdew, Burke, and Ernzerhof [17] (PBE) and the dispersion interactions were described with the D3BJ dispersion correction by Grimme et al. [18]. Calculations employed a mixed plane wave and Gaussian scheme using the Goedecker-Teter-Hutter pseudopotentials [19-21] for the ionic cores and the molecularly optimized short-range double-ζ plus polarization basis set to expand the Kohn-Sham orbitals of the valence electrons [22]. The density cutoff of 600 Ry was used in all calculations. In the structure optimizations the force convergence criteria was set to 0.023 eV $Å^{-1}$. The same density

cutoff and force convergence criteria have been used earlier to study pristine and nitrogen-doped CNTs [23].

The HER was modelled on the nitrogen-doped (14,0) carbon nanotube ($N_2$CNT). The model system contained two graphitic nitrogen atoms and 334 carbon atoms. The length of $N_2$CNT was 25.64 Å and the other two lattice parameters were 40 Å. In all calculations, only the Γ point has been used. The Volmer and Heyrovský reactions were investigated with the climbing image nudged elastic band (NEB) method [24]. The force criteria in the NEB calculations was 0.1 eV $Å^{-1}$.

The hydrogen adsorption Gibbs free energies, $\Delta G_{ads}$, were calculated in a gas phase, while the NEB calculations employed a water cluster of 33 water molecules. The water cluster model was validated with two different studies, see Supplementary Information for the related discussion. Similar approach to treat the water and surface has been earlier used by Holmberg and Laasonen [23,25]. First, the initial and final reaction configurations were created. It was started by relaxing the final configuration of the Volmer reaction. After that, the adsorbed hydrogen was moved to the closest water molecule above so that the Zundel cation, $H_5O_2^+$, was formed. Then the Zundel cation, the adsorption site and the carbon atoms within two bonds from the adsorption site were allowed to relax holding the water cluster at the fixed position. Secondly, the initial and final configurations for the Heyrovský reaction was created. The initial configuration was done by first optimizing the whole system and then the Zundel cation was formed by adding a hydrogen atom into the water cluster. Then the Zundel cation, the adsorption site and the carbon atoms within two bonds from the adsorption site were allowed to relax holding the water cluster at the fixed position. It should be noted that the distance between the reactive and adsorbed proton was ~ 2.30 Å in the initial conditions.

## 3 Theoretical background of hydrogen evolution reaction

It is generally accepted that hydrogen evolution under acidic conditions consist of the following steps:

1. Proton adsorption with charge transfer (the Volmer reaction):

$$H_3O^+ + e^- + * \rightarrow * H_{ads} + H_2O. \quad (1)$$

2. Combination of a surface hydrogen atom and a solvated proton (the Heyrovský reaction):

$$* H_{ads} + H_3O^+ + e^- \rightarrow * + H_2 + H_2O. \quad (2)$$

3. Combination of surface hydrogen atoms (the Tafel reaction):

$$* H_{ads} + * H_{ads} \rightarrow 2 * + H_2. \quad (3)$$

In the equations 1-3, * denotes the active free surface sites of the catalyst while $*H_{ads}$ is adsorbed hydrogen atom on the catalyst site. The HER begins with electrochemical adsorption of protons (the Volmer reaction) and is continued either with the combination of an adsorbed hydrogen atom and a solvated proton (the Heyrovský reaction) or with the combination of two adsorbed hydrogen atoms (the Tafel reaction). The mechanism depends on the kinetics of the reaction on the selected catalyst material. The rate-determining step (RDS), on the other hand, can depend also on the applied overpotential as the fraction of the active sites covered by adsorbed hydrogen is expected to increase with the overpotential.

According to previous measurements and modelling of the kinetics [26,27], the Tafel slope for the HER is 30 mV $dec^{-1}$ at low overpotentials if the reaction proceeds through the Volmer reaction followed by the Tafel reaction, where the former is the RDS. At high overpotentials the hydrogen surface coverage is high and the reaction is kinetically limited by the chemical Tafel reaction and hence, it is independent of the potential. Correspondingly, for the HER reaction proceeding *via* the Volmer reaction followed by the Heyrovský reaction, a Tafel slope of 40 mV $dec^{-1}$ is obtained at low overpotentials. For this Volmer-Heyrovský mechanism, at high overpotentials the Tafel slope is 120 mV $dec^{-1}$.

In addition to the above-discussed Tafel slope analysis, another diagnostic criteria for determining the HER reaction mechanism is variation of the reaction rate with pH. With high overpotentials (high surface proton coverage) the reaction rate increases ten-fold when the pH decreases one unit

if the reaction occur *via* the Volmer-Heyrovský mechanism. On the other hand, the reaction rate is independent of pH in the case of the Volmer-Tafel mechanism. [28]

# 4 Results

## 4.1 Characterization of the catalysts

Fig. 1 shows high-resolution magnification TEM micrographs of N-FWCNTs compared to pristine FWCNTs. Pristine FWCNTs comprise of few layers of highly graphitized structure (Figure 1a). Upon functionalization more surface defects are created on N-FWCNTs (yellow arrows). In addition, thin layer around the nanotubes resembling the graphitized polymer layer is wrapped around the nanotubes walls (noted in red ellipse).

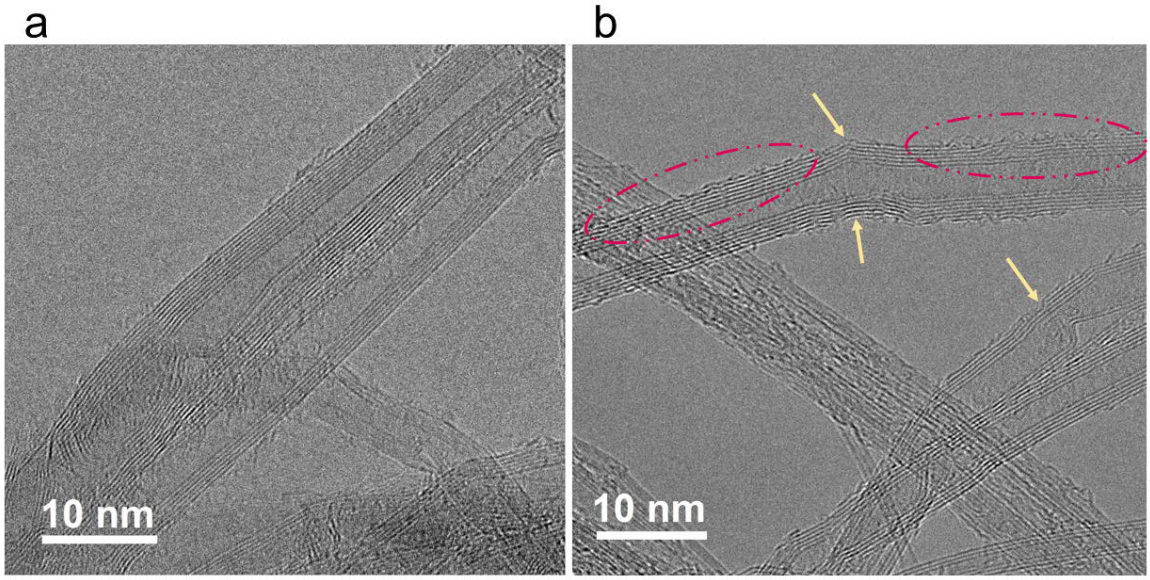


Figure 1. TEM micrographs of FWCNTs (a) and N-FWCNT-6 (b). Red circles show graphitized N-doped carbon layers and yellow arrows show surface defects on the walls.

The Raman spectra of the N-doped FWCNTs are depicted in comparison to the pristine FWCNTs in Fig. S1 (see Supporting Information). The D-band around 1350 $cm^{-1}$ is the characteristic mode for defective structures, and the G-band around 1580 $cm^{-1}$ corresponds to graphitic carbon [29]. N-doping of the FWCNTs results in downshift of G-band to lower frequencies as expected [12] and this shift can be attributed to C-C expansion (or contraction) and the changes of electronic structure. The low ratio of D to G band intensity ($I_D/I_G$) for the pristine FWCNTs (0.14) indicates highly ordered structure of nanotubes, as also observed in TEM micrographs (Fig. 1). For the N-FWCNTs, $I_D/I_G$ are observed to be around similar range (0.13-0.15) even after functionalization and polymer treatment, because the pyrolysis at high temperature (900 °C) results in high degree of graphitization.

At low frequencies (150-300 $cm^{-1}$) in the Raman spectra, radial breathing mode (RBM) appears as a result of radial vibration of carbon atoms associated with the small diameter tubes (less than 2 nm) or with the inner tubes of the FWCNTs [30]. The RBM intensities are decreased considerably upon functionalization and coverage of graphitic carbon layer around the FWCNTs. The longer functionalization caused more damage and irregular distribution of $sp^3$ sites or enlargement of the tubes, which affect the translational symmetry of the tubes. As a result, the tube resonance is reduced.

XPS has been carried out to investigate the surface chemical composition of N-FWCNTs and total atomic concentrations of carbon, oxygen and nitrogen. These XPS results (Fig. 2 and Table S1) show that the oxygen content in N-FWCNT increases from 0.7 to 1.3 at% with 4 h to 8 h acid treatment time. The nitrogen content also increases accordingly resulting in 0.59, 0.70 and 0.74 at% for N-FWCNT-4, N-FWCNT-6 and N-FWCNT-8, respectively. This is expected, as more functional oxygen groups are available for anchoring PANI on the surface of FWCNTs. It is also noteworthy that no trace metal impurities is observed in the XPS spectra tough $CoMoO_x$@MgO has been used to catalyse the FWCNT growth [13].

The high-resolution N 1s spectra (Fig. 2a) have been deconvoluted assuming the presence of four types of N-functional groups: pyridinic-N (at ca. 398.3 eV), pyrrolic-N (at ca. 400.1 eV), graphitic-N (at ca. 400.9 eV) and pyridinic-N-oxides (at ca. 403-404 eV). [13] Notably, despite different acid treatment conditions the relative distribution of N-functional configurations is similar for all the samples; 25-29% for pyridinic-N, 12-13% for pyrrolic-N, 30-32% for graphitic-N and 29-30%

for N-oxide groups. The O 1s spectra in Fig. 2b indicate that oxygen is present in at least two forms with binding energies of roughly 531.5 eV and 533 eV, which can be related to C=O and C-O and/or OH-bonds, respectively.

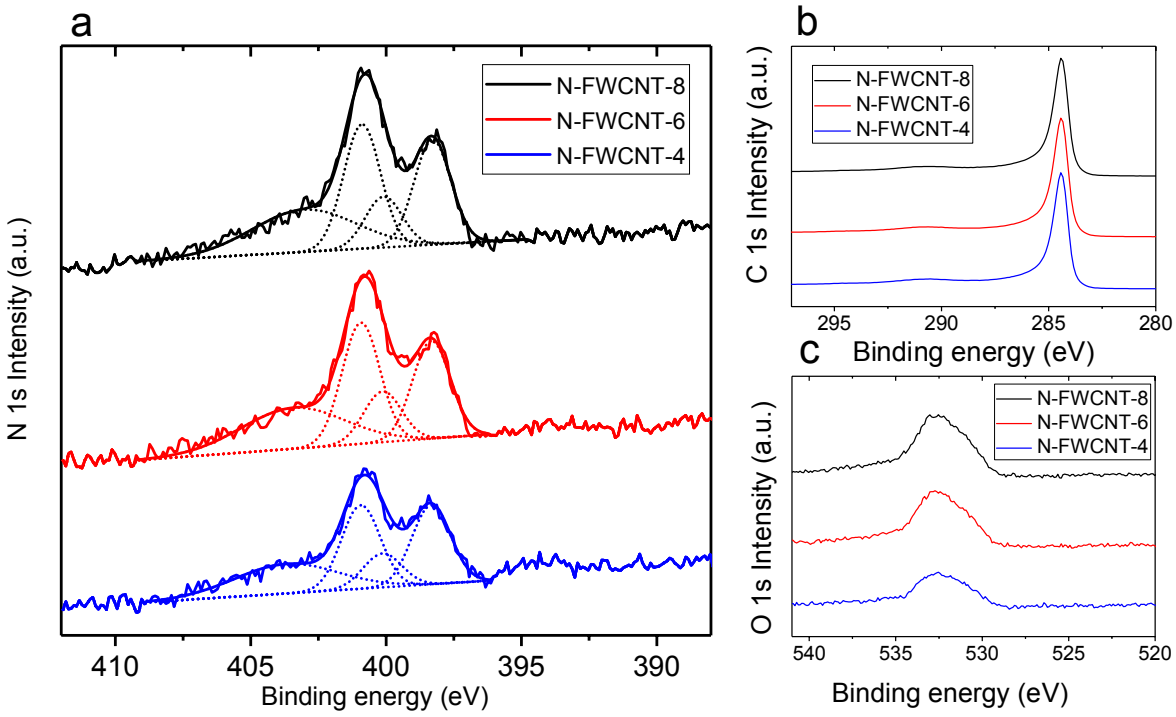


Figure 2. XPS spectra of a) nitrogen 1s b) carbon 1s and c) oxygen 1s for the investigated N-FWCNT samples. The nitrogen 1s spectra are shown together with the peak deconvolutions: pyridinic-N at ca. 398.3 eV, pyrrolic-N at ca. 400.1 eV, graphitic-N at ca. 400.9 eV and pyridinic-N-oxides at ca. 403-404 eV.

The results are summarized in Table S1 and different N-functional groups clarified in Fig. S2. Similar compositions may arise from the fact that all the samples have been pyrolyzed under the same conditions (900 °C, 2 h). As reported earlier [31], the pyrolysis temperature has the major influence on the formation of the final configurations of nitrogen functionalities. The dominant influence of pyrolysis temperature on N bonding configurations has also been observed in our previous study on N-graphene with different nitrogen precursors [32].

## 4.2 Electrochemical analysis of the catalysts

All three N-FWCNT catalysts show similar performance for the HER (Fig. 3): The onset overpotentials, to obtain 1 mA $cm^{-2}$ current, are 120-140 mV for each catalyst and the shape of the curves are alike to each other suggesting similar reaction mechanism. With N-FWCNT-4 fluctuation in the current is observed due to bubble formation and removal during hydrogen evolution on the electrode surface. In general, CNTs with shorter acid treatment period are more hydrophobic [33] and this plausibly result in favoring attachment of gas bubbles explaining the observed difference in the surface properties for the $H_2$ bubble removal. N-FWCNT-6 and N-FWCNT-8 show smooth curve, which is typical behavior for continuous removal of the produced hydrogen. At 400 mV overpotential the currents expand to a range from 55 to 62 mA $cm^{-2}$. These currents are still comparable to each other taking into account variance in electrode preparation.

The obtained current density of 19 mA $cm^{-2}$ at 300 mV overpotential is significantly higher than 5.5 mA $cm^{-2}$ previously reported for N-doped carbon catalyst in acidic media [11]. 250 mV overpotential is required to reach 10 mA $cm^{-2}$ current density, alas, this is higher than 120-220 mV overpotentials reported for the state-of-the-art non-noble metal HER catalysts such as $Ni_2P$, $MoS_2$ and $Mo_2C$ [34-41]

For comparison, also the HER on pristine and acid treated FWCNTs as well as on a commercial 60 wt% Pt/C samples are shown in Fig. 3a. Clearly pristine and acid treated FWCNTs show no notable activity for the HER as the obtained currents at overpotentials up to 400 mV are significantly lower than for the nitrogen-functionalized samples. This indicates the crucial role of the nitrogen functionalities for creating active sites for electrocatalyzing the HER.

The Tafel slopes with background corrected currents (Fig. 3b) obtained from potential range 160 to 200 mV are 116, 114 and 128 mV $dec^{-1}$ for N-FWCNT-4, N-FWCNT-6 and N-FWCNT-8, respectively. These are close to 120 mV $dec^{-1}$ suggesting that the reaction occurs mostly *via* the Volmer-Heyrovský mechanism with a fast proton adsorption followed by a slow electrochemical desorption step. This is anticipated to result from the structure of the catalysts where only the N-doped regions are active for the HER and the amount of the nitrogen functional groups is low. Moreover, it is plausible that protons are adsorbed exactly on top of a carbon atom (detailed discussion in section 4.5 Computation of hydrogen adsorption energies) affecting reaction mechanism. The chirality and bending of wall affects the C-C bond length in CNTs and 125 - 144

pm has been reported for single-walled CNTs [42] with similar dimeter range to FWCNTs used in this study. Hence, the C-C bond length, and the distance between the adjacent surface hydrogens, is notably longer than the H-H bond length (74 pm) hindering interaction between surface hydrogens. Consequently, for an adsorbed hydrogen atom there is no second surface hydrogen available in the vicinity and this prevents hydrogen molecule formation through the Tafel reaction. Consequently, the reaction can proceed only by interaction with a surface hydrogen and a solvated proton.

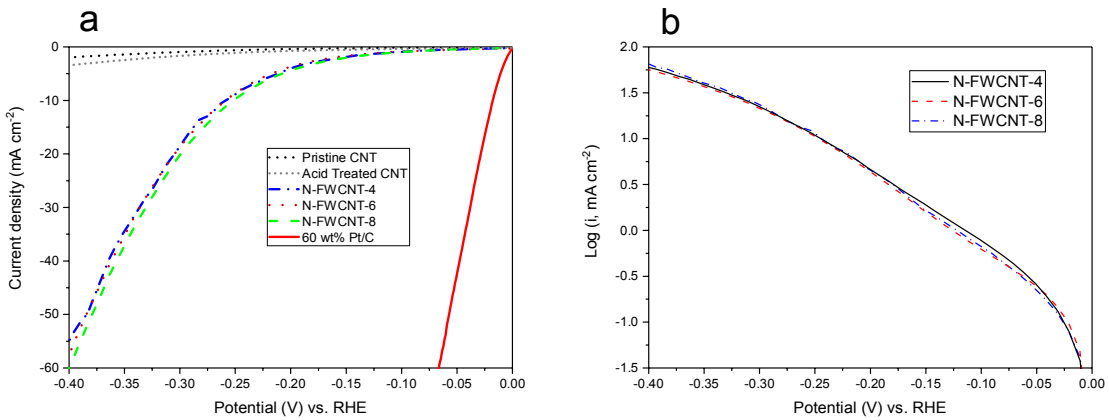


Figure 3. The HER polarization curves (a) and Tafel plots (b) for the N-FWCNT-4, N-FWCNT-6, N-FWCNT-8 catalysts in 0.5 M $H_2SO_4$, 3000 rpm rotation, 10 mV $s^{-1}$ scan rate. Acid treated FWCNT, pristine FWCNT and 60 wt% Pt/C references are shown in (a).

## 4.3 HER reaction mechanism analysis

As the electrocatalytic activity and mechanism of the HER on N- FWCNTs are similar only one of the samples, N-FWCNT-8, is selected for further studies.

The HER activity has been measured with different pH electrolyte solutions to analyze the reaction mechanism of the HER as discussed in section 3. Theoretical background. Polarization curves for the HER on the N-FWCNT-8 catalyst in $H_2SO_4$ pH series are shown in Fig. 4a. The HER current is constantly enhanced as the pH is decreasing from 1.5 to 0.3. The Tafel slopes with background

corrected currents (Fig. 4b), calculated from potential range 160 to 200 mV, show values of 187, 136, 125 and 120 mV $dec^{-1}$ for pH 1.5, 1, 0.6 and 0.3, respectively. This trend of approaching value of 120 mV $dec^{-1}$, which is the theoretical value for the Volmer-Heyrovský reaction, suggests that proton concentration in the electrolyte affects the reaction mechanism of the HER on N-FWCNT. Increased availability of protons in the electrolyte can increase the hydrogen coverage on the surface (the Volmer reaction) and in addition facilitate the reaction of an adsorbed hydrogen atom with a solvated proton (the Heyrovský reaction).

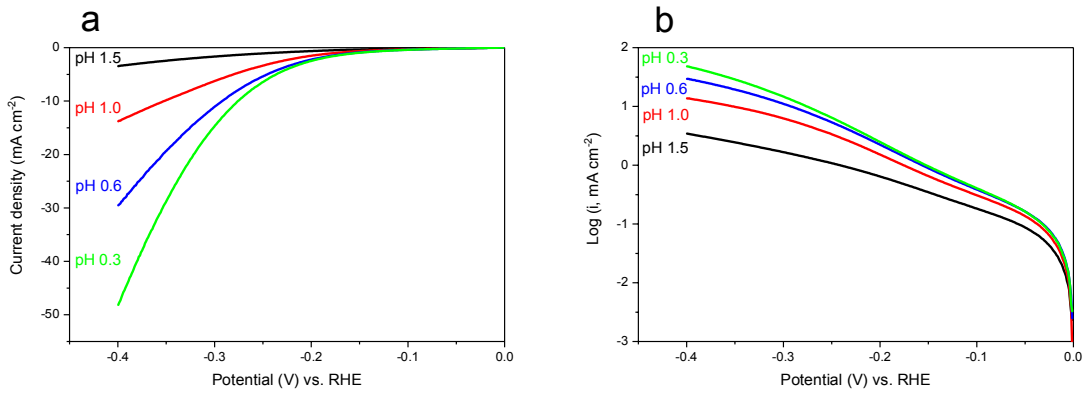


Figure 4. Polarization curves for the hydrogen evolution on N-FWCNT-8 in $H_2SO_4$ pH series (a) and respective Tafel slopes (b) measured at $v$ = 10 mV $s^{-1}$, rotation 3000 rpm.

The slope of the log $i$ vs. pH (Fig. 5a) at low overpotentials is around 0.2 and arise close to 1 with increasing overpotential (Fig. 5b). This behavior implies that the reaction mechanism is not well defined at low overpotentials with low HER currents. As the overpotential is increased and thus the hydrogen surface coverage enhanced, the reaction is dominated by the Volmer-Heyrovský reaction suggested by the slope value approaching 1. The same phenomenon is observed for the Tafel slopes (Fig. 3b) as increased hydrogen coverage enhances the Volmer-Heyrovský mechanism.

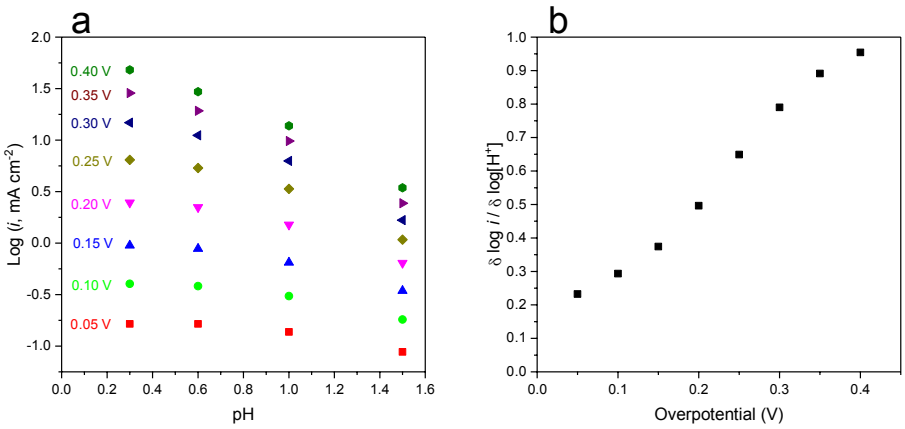


Figure 5. The linear slopes of the log *i* vs. pH at chosen overpotentials (a) and the log *i*/pH slopes *vs*. chosen overpotentials for the N-FWCNT-8 catalyst in the low-pH sulfuric acid electrolytes (b).

To better understand the processes taking place during the HER, electrochemical impedance spectroscopy has been carried out under different overpotentials with N-FWCNT-8. The Bode plots (Fig. 6a) reveal typical single time constant behavior related to smooth surfaces with one dominant reaction whereas multiple time constants would suggest a porous and rough electrode surface. The equivalent circuit model for the single time constant is described as a series resistance ($R_s$) in series with a charge transfer process containing parallel double layer capacitance ($C_{dl}$) and charge transfer resistance ($R_{ct}$). The Nyquist plot of the measured data (Fig. 6b) reveals the $R_s$ values (the high-frequency end intersection section with the Z' axes) as 5.2 and 5.5 Ohm for 0 mV and 200 mV overpotentials, respectively. At 0 mV overpotential charge transfer resistance cannot be observed as the HER does not progress facilely. At 200 mV overpotential the charge transfer value is circa 97 Ohm, which is similar to other reported values for the HER with non-noble metal catalysts at similar potentials and current densities [43-46].

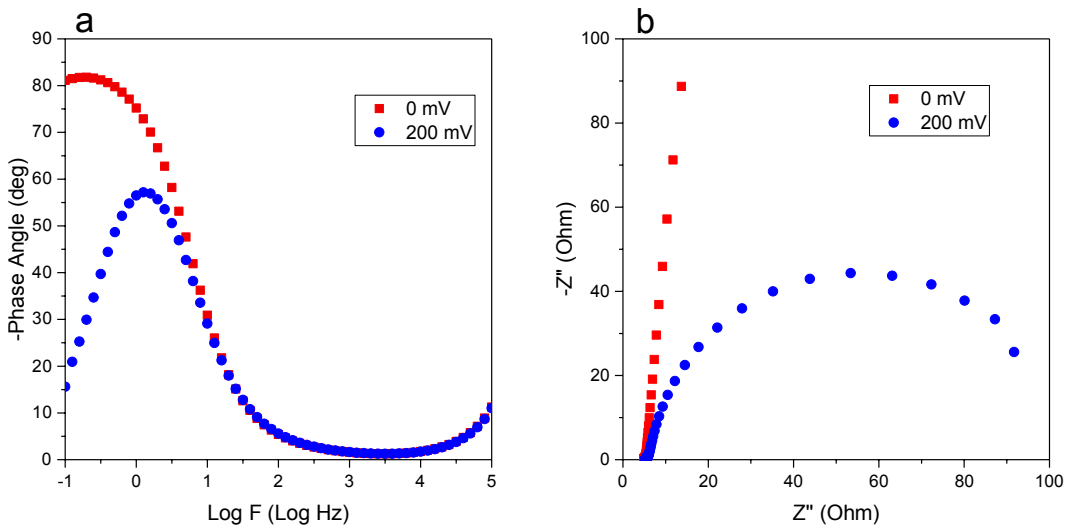


Figure 6. The Bode (a) and the Nyquist (b) plots of the impedance analysis for the catalyst N-FWCNT-8 with 0 and 200 mV overpotentials.

## 4.4 Validation of the catalyst durability and usability

Aging and stability of N-FWCNT-8 has been investigated with continuous cyclic voltammogram measurements. After cycling potential between 0.1 V and -0.4 V for 100 times N-FWCNT-8 retains its catalytic properties for the HER as no decrease in the current is observed (Fig. 7). Only difference in the polarization curves is fluctuation of the current resulting from bubble formation and removal.

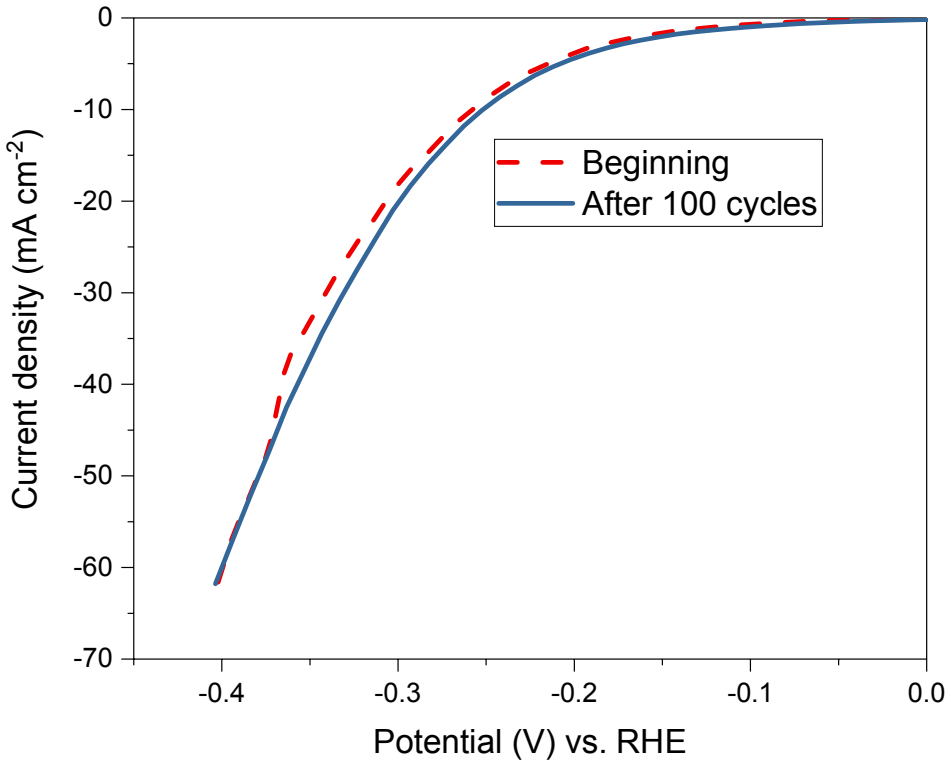


Figure 7. Polarization curve of N-FWCNT-8 at the beginning of the experiments and after 100 cycles in 0.5 M $H_2SO_4$, 3000 rpm rotation, 10 mV $s^{-1}$ scan rate.

Validation of N-FWCNTs suitability for electrolyzer systems have been measured with a methanol electrolyzer cell. The onset potential is higher for N-FWCNT-8 than for Pt/C but in contrary the HER currents increases steeper and approaching those of Pt/C when overpotential is increased (Fig. S3). N-FWCNT-8 showed stable performance with varying temperatures at the range of 30 ºC – 70 ºC and over five weeks of operation at 30 ºC. Thus, these results prove suitability of N-FWCNTs for electrolyzer systems (Fig. S5). Detailed description of the experimental methods and results are presented in Supporting Information.

## 4.5 Computation of hydrogen adsorption energies

The HER is initiated by the Volmer reaction as already mentioned above in section 3. Theoretical background. Therefore, the computational investigation of the reaction mechanism is started by hydrogen adsorption free energy calculations, $\Delta G_{ads}$, as $\Delta G_{ads} = \Delta E_{ads} + 0.25$ eV for different adsorption sites on the nitrogen doped CNTs (Fig. 8). Graphitic nitrogen sites are selected for these computational studies because their fraction of the various nitrogen moieties is the highest (see Table S2 and related discussion in section 3.1 Catalyst structure). Moreover, the N concentration in the selected system is ~0.5 at%, which is slightly lower than 0.59 – 0.74 at% detected by XPS in the N-FWCNTs used in the experiments (see Fig. 2 and related discussion). $\Delta G_{ads}$ is calculated for 12 adsorption sites including two graphitic nitrogen atoms (Table 1), and this system is referred as $N_2$CNT. The used CNT is (14,0). The $\Delta G_{ads}$ is a simple model for estimating the most active sites for the HER, see Supplementary Information for calculating $\Delta G_{ads}$. Based on calculation of Pt [47] the target value for $\Delta G_{ads}$ is ca. 0 eV. Our calculations reveal that the single H active sites are located on the carbon atoms between the nitrogen atoms (C1 and C2), as can be expected, and their $\Delta G_{ads}$ is 0.23 eV. C5 and C9, located next to the nitrogen atom, are less active than the sites between the nitrogen atoms. For other sites, $\Delta G_{ads}$ is more endothermic making hydrogen adsorption to them less probable. In addition, it should be noted that the adsorption does not take place onto the nitrogen atoms. Based on these hydrogen adsorption calculations, C1 site has been selected as an example of an active site in $N_2$CNT.

Hydrogen adsorption energy calculations at higher coverages are performed with different hydrogen surface configurations [23,25]. C1 site is always occupied and 17 different configurations have been selected for the calculations and their adsorption energies are transformed into $\Delta G_{ads}$. The calculated $\Delta E_{ads}$ and $\Delta G_{ads}$ for each site are reported in Table 2 and from these results, it can be noted that the occupation of C1 site will increase significantly the adsorption on C2 site but it will have rather weak influence to the other sites. When both C1 and C2 sites are occupied the effect to other adsorption sites are substantial but rather complex.

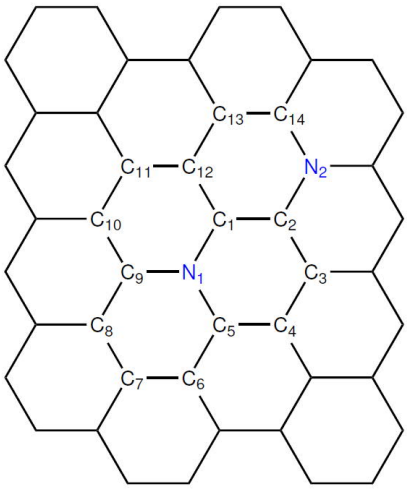


Figure 8. The numbered adsorption sites on the surface of $N_2$CNT.

Table 1. Calculated hydrogen adsorption energies ($\Delta E_{ads}$) and Gibbs free energies ($\Delta G_{ads}$) for $N_2$CNT. $\Delta G_{ads}$ is corrected as $\Delta G_{ads} = \Delta E_{ads} + 0.25$ eV.

| Adsorption site | $\Delta E_{ads}$ (eV) | $\Delta G_{ads}$ (eV) |
|---|---|---|
| C1 | -0.02 | 0.23 |
| C2 | -0.02 | 0.23 |
| C5 | 0.06 | 0.31 |
| C6 | 0.61 | 0.86 |
| C7 | 0.25 | 0.50 |
| C8 | 0.55 | 0.80 |
| C9 | 0.12 | 0.37 |
| C10 | 0.39 | 0.64 |
| C11 | 0.36 | 0.61 |
| C12 | 0.19 | 0.44 |
| N1 | 1.29 | 1.54 |
| N2 | 1.29 | 1.54 |

Table 2. Calculated hydrogen adsorption energies ($\Delta E_{ads}$) and Gibbs free energies ($\Delta G_{ads}$) when the C1 site is occupied. $\Delta G_{ads}$ is corrected as $\Delta G_{ads} = \Delta E_{ads} + 0.25$ eV. All energies are per hydrogen atom.

| Additional occupied site(s) | $\Delta E_{ads}$ (eV) | $\Delta G_{ads}$ |
|---|---|---|
| C2 | -0.41 | -0.16 |
| C3 | 0.20 | 0.45 |
| C4 | 0.27 | 0.52 |
| C9 | 0.08 | 0.33 |
| C10 | 0.28 | 0.53 |
| C11 | 0.28 | 0.53 |
| C12 | 0.14 | 0.39 |
| C13 | 0.14 | 0.39 |
| C14 | 0.02 | 0.27 |
| C2 C5 | -0.14 | -0.11 |
| C2 C12 | -0.16 | -0.09 |
| C5 C9 | 0.26 | 0.51 |
| C5 C12 | 0.30 | 0.55 |
| C2 C5 C9 C10 | -0.02 | 0.23 |
| C2 C5 C9 C11 | 0.24 | 0.49 |
| C2 C5 C9 C12 | -0.06 | 0.19 |
| C2–C5 C9–C14 | 0.04 | 0.29 |

## 4.6 Reaction Barrier Calculations

Quite often new HER catalysts are studied using only $\Delta G_{ads}$ as done above. $\Delta G_{ads}$, however, does not provide any information about barriers involved in reactions. Therefore, these barriers for the Volmer and Heyrovský reactions are investigated here using a water cluster and employing the NEB method [24]. For the NEB calculations, the clean surface without and with different charge states, and with different hydrogen configurations using the C1 site as the active site is selected. First only hydrogen at C1 site and then two extremes have been considered, namely the configurations, which produced the most exothermic and endothermic adsorption energies.

As discussed above, the Volmer reaction is the initial reaction of the HER where the proton is adsorbed onto the surface. For the proton adsorption, a reaction barrier of 0.11 eV is found (Fig. 9). To study the effect of increasing negative charge, the NEB path of the neutral system has been reoptimisez with the charge states of q =−1 and −2. The increasing negative charge makes the Volmer reaction barrier decrease until it disappeared with the charge of $q = -2$. In case of the Heyrovský reaction, the barrier is calculated to be 1.19 eV. Adding negative charge to the system, the reaction barrier is found to decrease to 1.06 and 0.94 eV with $q = -1$ and −2, respectively. After identifying the hydrogen coverages producing the most exothermic (C2 C5 C9 C12) and endothermic (C5 C9) adsorption energies, NEB calculations are performed with these coverages. The energies of the NEB calculations are shown in Fig. 10. These results clearly show a strong influence of the surface coverage on the reaction barriers to the Volmer reaction. As it can be seen in Fig. 10, the most exothermic case show no reaction barrier at all whereas the endothermic case has a reaction barrier of 0.74 eV.

In case of the second reaction step, the Heyrovský reaction, the exothermic case show an unexpected result. The reaction barrier for this is expected to be larger than for the clean surface due to the strong hydrogen adsorption in the gas phase calculations (Tables 1 and 2) but the results shows that their reaction barriers are the same within the GGA functional accuracy. Correspondingly, the endothermic adsorption energy has the smallest reaction barrier. Based on these calculations, Brønsted-Evans-Polanyi relationship (BEP) figures are constructed and the related discussion can be found in Supplementary Information. So far, only a single site in the NEB calculations has been considered and no strong conclusion can be made.

The Heyrovský reaction has been forced to take place between the solvated proton and adsorbed hydrogen on the C1 site. Sometimes, however, the modelled reaction path does not reflect the best path to the products. Therefore, an alternative reaction path to the molecular hydrogen is investigated using a different active site instead of the C1 site. For this calculation, the C12 site with the hydrogen coverage producing the most exothermic adsorption energy is selected. This allows a direct comparison of the reaction barriers with each other. For the C12 site, a reaction barrier of only 0.64 eV is found and the alternative path is shown in Fig. 10b (cyan). The significance of these results is discussed in the next chapter.

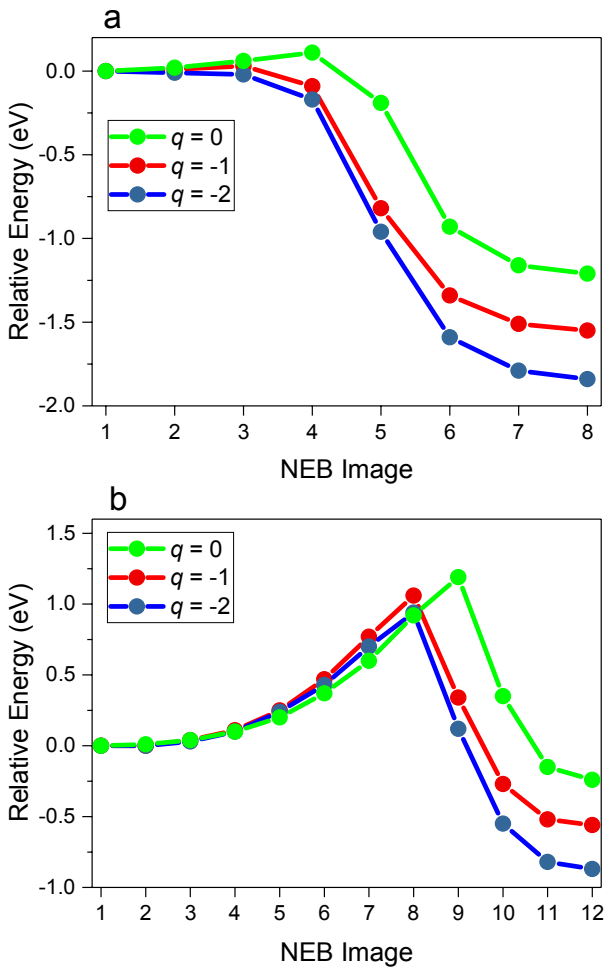


Figure 9. The graphical representations of the optimized NEB bands of the Volmer (a) and the Heyrovský (b) reactions at C1 site.

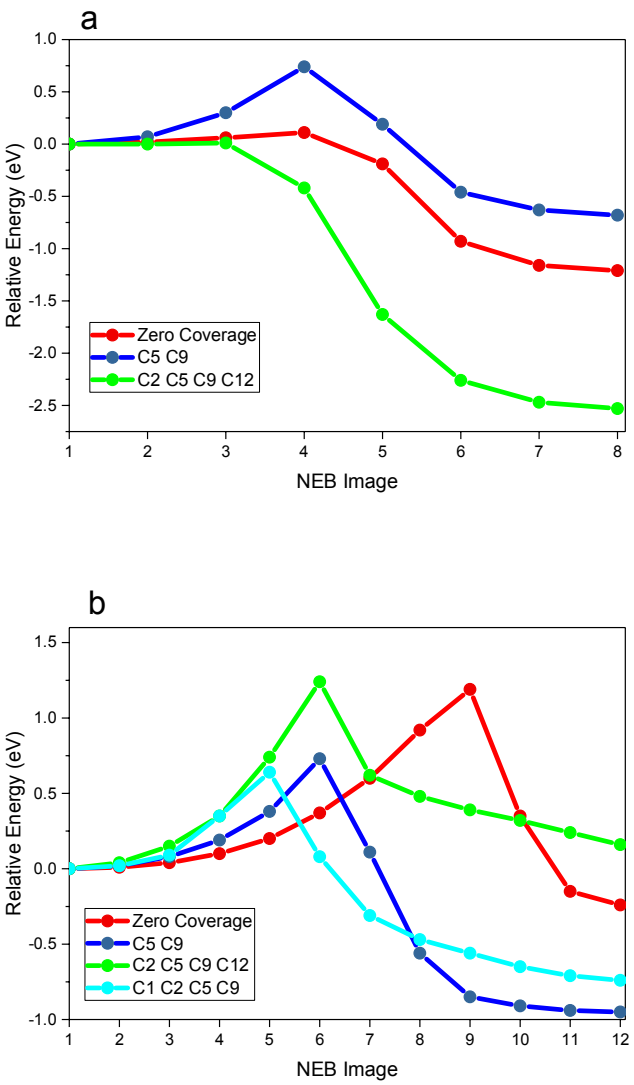


Figure 10. The graphical representations of the optimized NEB bands of the Volmer (a) and Heyrovský (b) reactions. The occupied sites are indicated in the figure. The cyan line corresponds to the alternative C12 reaction site. For other configurations, the active site is C1.

## 4.7 Analysis of the computational results

The low surface coverage calculations of $N_2$CNT show that the reaction barrier for the rate-determining reaction is 1.19 eV. This is 0.10 eV larger than the corresponding reaction barrier for the pristine CNT [23]. This is in agreement with our earlier results that a single graphitic nitrogen atom in carbon nanotube (NCNT) actually decrease activity [23]. However, in the previous study only few reaction barriers have been investigated. Based on the data presented here the situation is more complex. Introducing electrons to the neutral system decrease reaction barriers of the Heyrovský reaction making it more favorable. However, even with $q = -2$ the reaction barrier is still rather high, 0.94 eV, suggesting that the reaction is not very fast.

The hydrogen coverage seems to have a strong influence on the adsorption energies, which can explain the slow increase of the current density in the low overpotentials (see Fig. 3). These observations suggests that hydrogen evolution is preceded by hydrogen overpotential adsorption. Quite unexpectedly, the hydrogen coverage with the most exothermic adsorption energy showed similar reaction barrier to that of the C1 site. Clearly, adsorption energies do not fully explain the activity of $N_2$CNT. Therefore, one should be careful if the activity analyses are based on $\Delta G_{ads}$ only. The hydrogen coverage with the most endothermic $\Delta G_{ads}$ seems to have the most promising reaction barrier for the HER.

Often the reactions are studied using a single active site for every calculation because the number of adsorption site combinations will increase in large systems making the study more difficult. In this study, an alternative reaction path has been modelled to investigate if it has an influence on the reaction barriers. Here, the C12 site has been selected to represent another active site because it has rather low energy when the sites C1, C2, C5 and C9 are occupied. The same initial configuration is used, which makes direct comparison of the two calculated reaction paths possible. The NEB calculation produced a notably lower barrier of 0.64 eV for this reaction path. The lower reaction barrier is interesting since it has precisely the same initial configuration as the path to C1 site. Naturally, it is more reasonable that the reaction takes place through the reaction path with the lower barrier. This result is interesting because the active site is not next to the nitrogen atom. Hence, a valid question is the role of nitrogen atom(s) in the HER. To answer this question, the same NEB band is reoptimized using the same NEB trajectory but replacing one nitrogen atom with a carbon atom. In this case, the reaction barrier is found to decrease to 0.58 eV. This is 0.06

eV lower than with two graphitic nitrogen atoms, which means that it is within the accuracy of GGA functionals. Therefore, conclusion on the difference between the described system with one and two graphitic nitrogen atoms cannot be made but in any case the reaction barriers are significantly lower than in the case of undoped CNT. This is very significant result, which confirms the experimentally obtained catalytic activity enhancing effect of N-doping in CNT.

Due to the superior activity of platinum for the HER, it is good to compare these calculations also with those for platinum. It should be noted that the calculations on platinum have shown notable differences with the experiments, which makes the comparison more challenging. For example, the calculated reaction barrier for the Tafel reaction, which is the rate-determining reaction on platinum, show a reaction barrier of 0.85 eV [48]. This is 0.65 eV higher than the experimentally determined value for Pt(111) [49]. In addition, the calculations in ref. 44 treat water with ice-like bilayer that includes the hydronium ion. This approach is different from our water cluster model, which makes the comparison of these two calculations challenging. Therefore, it would be more reasonable to compare our calculations with the experiments which reveal notably higher HER activity on platinum than on N-FWCNT (Fig. 3) as can be expected. Furthermore, the experiments show that the N-FWCNT is clearly more active than pristine CNT, and this is in good agreement with the calculations because the calculated reaction barrier (ca. 1 eV) of pristine CNT is much higher than the N-doped CNT barriers (ca. 0.6 eV).

## 5 Conclusions

Earth-abundant element based N-FWCNTs exhibit a high activity towards the catalysis of the HER in an acidic electrolyte and the material is highly competitive compared to other experimental electrocatalysts reaching roughly similar HER current densities as e.g. $Ni_2P$, $MoS_2$ and $Mo_2C$. Obtained Tafel slope is close to 120 mV $dec^{-1}$, indicative of a Volmer-Heyrovský type mechanism, which is supported by computational investigations.

Spin-polarized density functional theory calculations showed that the rate-determining reaction barrier is large on the adsorbent free surface, which implies that the HER is initiated when the surface coverage is increased. Reaching certain surface hydrogen coverage is a plausible explanation for the experimental observation that the HER on-set potential on N-FWCNT is located at negative potential from the thermodynamical one. These calculations also show that the

Heyrovský reaction is the rate-determining reaction in the HER, which is in agreement with the experimental studies carried out at low pH.

The calculations suggest that there might be also alternative reaction paths on carbons located at different distances from nitrogen, which provide more favorable path to the hydrogen evolution. Based on this investigation, it can be concluded that nitrogen-doping clearly has an effect on the reaction barriers making CNT more active towards the HER as shown experimentally, as well.

The PEM electrolysis cell utilizing N-FWCNTs has a HER onset overpotential of approximately 300 mV and performs with a high stability and efficiency, reaching current densities and production rates competitive with a conventional platinum catalyst. Decrease in the currents over time can be observed which can originate from many different phenomena occurring at both the electrodes. Further research is required to analyze the mechanism of the erosion and enabling alterations to the manufacturing process to enhance N-FWCNT durability.

In a broader context, our findings suggest that this kind of a complex catalyst material has several active sites with different reaction barriers for promoting the electrochemical reaction. This is an interesting observation as, for example, in numerous studies on oxygen reduction reaction on nitrogen doped carbon nanomaterials carbon atoms located next to nitrogen have been suggested as the active sites but carbons located further away have not been considered. Careful screening of different reaction sites could also shed new light for understanding this multi-step reaction on a complex electrocatalyst surface.

This study highlights once again that by combination of experimental and computational results yield valuable information of the reaction mechanism in different conditions and reveals the catalytically active surface sites in the catalysts. This is crucial information required for optimizing the catalyst structure and the reaction conditions when developing electrocatalysts for electrolyzers.

## 6 Acknowledgements

Dr. Garold Murdachaew is acknowledged for helpful discussions during this research and Mr. Nico Holmberg, M. Sc. (Tech.), is acknowledged for providing his version of the Quickstep/CP2K software and a useful script for the nudged elastic band calculations. Dr. Ilya Anoshkin is thanked for synthetizing CNTs. The authors thank for the DEMEC, CIRCLE and CloseLoop projects of

Academy of Finland (n:o 13286266, 13303949, 13303452). In addition, the Ministry of Education and Science of the Russian Federation in the framework of increase Competitiveness Program of NUST "MISIS" (project is K3-2017-039) is acknowledged for funding. AGN thanks the support by Skoltech NGP Program (Skoltech-MIT joint project). This work made use of the Aalto University Nanomicroscopy Center (Aalto-NMC) premises and the RAMI RawMaterial Infrastructure. The computer resources were provided by CSC – the Finnish IT Centre for Science.

## 7 Supporting information

Characterization data, electrolyzer measurements, computational details

## 8 References

1. Renewables 2016 global status report. (2017). REN21. Retrieved from www.ren21.net/

2. Tavakkoli, M., Kallio, T., Reynaud, O., Nasibulin, A. G., Johans, C., Sainio, J., Jiang, H., Kauppinen, E. I., & Laasonen, K., *Angewandte Chemie International Edition,* 54 (2015) 4535-4538.

3. Deng, J., Ren, P., Deng, D., Yu, L., Yang, F., & Bao, X., *Energy Environ.Sci.,* 7 (2014) 1919-1923.

4. Liu, Q., Tian, J., Cui, W., Jiang, P., Cheng, N., Asiri, A. M., & Sun, X., *Angewandte Chemie,* 126 (2014) 6828-6832.

5. Youn, D. H., Han, S., Kim, J. Y., Kim, J. Y., Park, H., Choi, S. H., & Lee, J. S., *ACS Nano,* 8 (2014) 5164-5173.

6. Wang, D., Gong, M., Chou, H., Pan, C., Chen, H., Wu, Y., Lin, M., Guan, M., Yang, J., Chen, C., Wang, Y., Hwang, B., Chen, C., & Dai, H., *J.Am.Chem.Soc.,* 137 (2015) 1587-1592.

7. Chen, Z., Higgins, D., & Chen, Z., *Electrochim.Acta,* 55 (2010) 4799-4804.

8. Geng, D., Liu, H., Chen, Y., Li, R., Sun, X., Ye, S., & Knights, S., *J.Power Sources,* 196 (2011) 1795-1801.

9. Kundu, S., Nagaiah, T. C., Xia, W., Wang, Y., Dommele, S. V., Bitter, J. H., Santa, M., Grundmeier, G., Bron, M., Schuhmann, W., & Muhler, M., *J.Phys.Chem.C,* 113 (2009) 14302-14310.

10. Nagaiah, T. C., Kundu, S., Bron, M., Muhler, M., & Schuhmann, W., *Electrochemistry Communications,* 12 (2010) 338-341.

11. Long, G., Wan, K., Liu, M., Liang, Z., Piao, J., & Tsiakaras, P., *Journal of Catalysis,* 348 (2017) 151-159.

12. Davodi, F., Tavakkoli, M., Lahtinen, J., & Kallio, T.Straightforward synthesis of nitrogen-doped carbon nanotubes as highly active bifunctional electrocatalysts for full water splitting (2017) 19-27.

13. Borghei, M., Kanninen, P., Lundahl, M., Susi, T., Sainio, J., Anoshkin, I., Nasibulin, A., Kallio, T., Tammeveski, K., Kauppinen, E., & Ruiz, V., *Applied Catalysis B: Environmental,* 158–159 (2014) 233-241.

14. the CP2K developers group. (2015). CP2K version 2.7 (development version). Retrieved from http://www.cp2k.org/

15. Hutter, J., Iannuzzi, M., Schiffmann, F., & VandeVondele, J., *Wiley Interdisciplinary Reviews: Computational Molecular Science,* 4 (2014) 15-25.

16. Van de Vondele, J., Krack, M., Mohamed, F., Parrinello, M., Chassaing, T., & Hutter, J., *Comput.Phys.Commun.,* 167 (2005) 103-128.

17. Perdew, J. P., Burke, K., & Ernzerhof, M., *Phys.Rev.Lett.,* 77 (1996) 3865-3868.

18. Grimme, S., Ehrlich, S., & Goerigk, L., *Journal of Computational Chemistry,* 32 (2011) 1456-1465.

19. Goedecker, S., Teter, M., & Hutter, J., *Phys.Rev.B,* 54 (1996) 1703-1710.

20. Hartwigsen, C., Goedecker, S., & Hutter, J., *Phys.Rev.B,* 58 (1998) 3641-3662.

21. Krack, M., *Theoretical Chemistry Accounts,* 114 (2005) 145-152.

22. VandeVondele, J., & Hutter, J., *J.Chem.Phys.,* 127 (2007) 114105.

23. Holmberg, N., & Laasonen, K., *J.Phys.Chem.C,* 119 (2015) 16166-16178.

24. Henkelman, G., Uberuaga, B. P., & Jónsson, H., *J.Chem.Phys.,* 113 (2000) 9901-9904.

25. Holmberg, N., & Laasonen, K., *J.Phys.Chem.Lett.,* 6 (2015) 3956-3960.

26. Bockris, J. O., & Potter, E. C., *J. Electrochem. Soc.,* 99 (1952) 169-186.

27. Conway, B. E., & Tilak, B. V., *Electrochim.Acta,* 47 (2002) 3571-3594.

28. Tuomi, S., Guil-Lopez, R., & Kallio, T., *Journal of Catalysis,* 334 (2016) 102-109.

29. Dresselhaus, M. S., Dresselhaus, G., Saito, R., & Jorio, A.Raman spectroscopy of carbon nanotubes (2005) 47-99.

30. Graupner, R., *J.Raman Spectrosc.,* 38 (2007) 673-683.

31. Sharifi, T., Hu, G., Jia, X., & Wågberg, T., *ACS Nano,* 6 (2012) 8904-8912.

32. Borghei, M., Azcune, I., Carrasco, P. M., Sainio, J., Kauppinen, E., & Ruiz, V., *Int J Hydrogen Energy,* 39 (2014) 12749-12756.

33. Nasibulin, A. G., Kaskela, A., Mustonen, K., Anisimov, A. S., Ruiz, V., Kivistö, S., Rackauskas, S., Timmermans, M. Y., Pudas, M., Aitchison, B., Kauppinen, M., Brown, D. P., Okhotnikov, O. G., & Kauppinen, E. I., *ACS Nano,* 5 (2011) 3214-3221.

34. Yu, J., Zhou, W., Xiong, T., Wang, A., Chen, S., & Chu, B., *Nano Research,* 10 (2017) 2599-2609.

35. Merki, D., Vrubel, H., Rovelli, L., Fierro, S., & Hu, X., *Chem.Sci.,* 3 (2012) 2515-2525.

36. Feng, L., Vrubel, H., Bensimon, M., & Hu, X., *Phys.Chem.Chem.Phys.,* 16 (2014) 5917-5921.

37. Li, Y., Wang, H., Xie, L., Liang, Y., Hong, G., & Dai, H., *J.Am.Chem.Soc.,* 133 (2011) 7296-7299.

38. Vrubel, H., & Hu, X., *Angewandte Chemie,* 124 (2012) 12875-12878.

39. Faber, M. S., Dziedzic, R., Lukowski, M. A., Kaiser, N. S., Ding, Q., & Jin, S., *J.Am.Chem.Soc.,* 136 (2014) 10053-10061.

40. Zhou, W., Zhou, J., Zhou, Y., Lu, J., Zhou, K., Yang, L., Tang, Z., Li, L., & Chen, S., *Chem.Mater.,* 27 (2015) 2026-2032.

41. Yang, L., Zhou, W., Jia, J., Xiong, T., Zhou, K., Feng, C., Chen, *Carbon*, 122 (2017) 710-717.

42. Budyka, M. F., Zyubina, T. S., Ryabenko, A. G., Lin, S. H., & Mebel, A. M. *Chem. Phys. Letters*, 407 (2005). 266-271.

43. Chen, W., Wang, C., Sasaki, K., Marinkovic, N., Xu, W., Muckerman, J. T., Zhu, Y., & Adzic, R. R., *Energy Environ. Sci.,* 6 (2013) 943-951.

44. Liao, L., Wang, S., Xiao, J., Bian, X., Zhang, Y., Scanlon, M. D., Hu, X., Tang, Y., Liu, B., & Girault, H. H., *Energy Environ. Sci.,* 7 (2014) 387-392.

45. Xiao, P., Yan, Y., Ge, X., Liu, Z., Wang, J., & Wang, X., *Applied Catalysis B: Environmental,* 154–155 (2014) 232-237.

46. Alhajri, N. S., Anjum, D. H., & Takanabe, K., *J. Mater. Chem. A,* 2 (2014) 10548-10556.

47. Nørskov, J. K., Bligaard, T., Logadottir, A., Kitchin, J. R., Chen, J. G., Pandelov, S., & Stimming, U., *Journal of the Electrochemical Society,* 152 (2005) J23-J26.

48. Skúlason, E., Tripkovic, V., Björketun, M. E., Gudmundsdóttir, S., Karlberg, G., Rossmeisl, J., Bligaard, T., Jónsson, H., & Nørskov, J. K., *J.Phys.Chem.C,* 114 (2010) 18182-18197.

49. Marković, N. M., Grgur, B. N., & Ross, P. N., *J Phys Chem B,* 101 (1997) 5405-5413.

# Supporting Information

# Experimental and Computational Investigation of Hydrogen Evolution Reaction Mechanism on Nitrogen Functionalized Carbon Nanotubes

Sami Tuomi[a], Olli J. Pakkanen[b], Maryam Borghei[c,d], Rasmus Kronberg[a], Jani Sainio[e], Esko I. Kauppinen[d], Albert G. Nasibulin[f,d], Kari Laasonen[b], Tanja Kallio[a]*

[a] *Research Group of Electrochemical Energy Conversion and Storage, Department of Chemistry and Material Science, Aalto University, P.O. Box 16100, 00076 Aalto, Finland*

[b] *Research Group of Computational Chemistry, Department of Chemistry and Material Science, Aalto University, P.O. Box 16100, 00076 Aalto, Finland*

[c] *Bio-based Colloids and Materials, Department of Bioproducts and Biosystems, Aalto University, P.O. Box 16300, 00076 Aalto, Finland*

[d] *Department of Applied Physics, School of Science, Aalto University, P.O. Box 15100, FI-00076 Aalto, Finland*

[e] *Surface Science Group, Department of Applied Physics, Aalto University, P.O. Box 15100, 00076 Aalto, Finland*

[f] *Skolkovo Institute of Science and Technology, 100 Novaya str., Skolkovo, Moscow Region, 143025, Russia*

*Corresponding author. Tel.: +358 50 563 7567, Fax: +358 9 470 22580, E-mail address: tanja.kallio@aalto.fi

## 1 Characterization of the catalysts

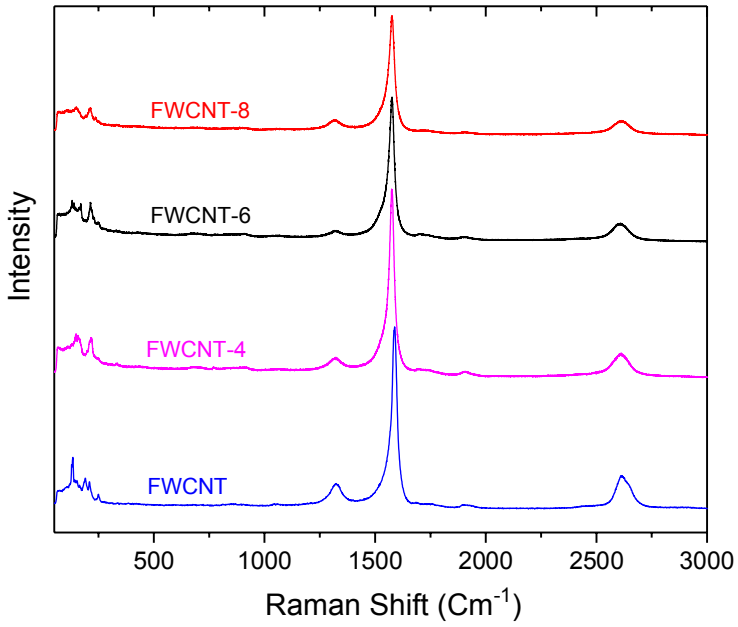


Figure S1. Raman spectra of N-FWCNTs and pristine FWCNTs.

Table S1. The atomic concentrations of N-FWCNTs according to XPS and the percentages of different nitrogen species of all nitrogen as derived from the peak deconvolutions. The error associated with each value is roughly ± 10% of the value.

| | Atomic concentration (%) | | | Percentages of N species of all nitrogen | | | |
|---|---|---|---|---|---|---|---|
| | C | O | N | Pyridinic | Pyrrolic | Graphitic | N-oxide |
| N-FWCNT-4 | 98.7 | 0.7 | 0.59 | 29 % | 12 % | 30 % | 29 % |
| N-FWCNT-6 | 98.3 | 1.0 | 0.70 | 25 % | 13 % | 32 % | 29 % |
| N-FWCNT-8 | 98.0 | 1.3 | 0.74 | 26 % | 13 % | 31 % | 30 % |

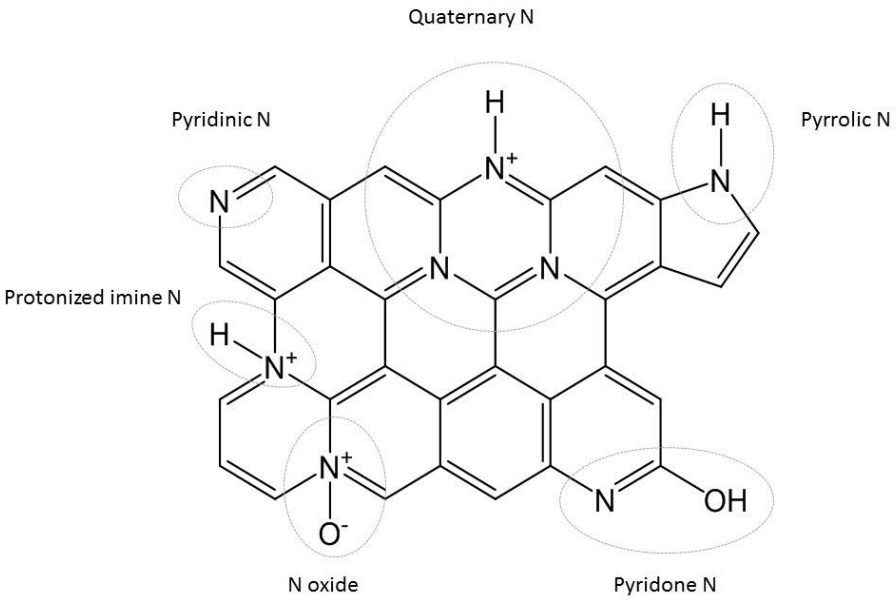


Figure S2. Nitrogen functional groups in CNT structure.

## 2 Electrolyzer cell measurements

### 2.1 Electrolyzer cell experimental

Electrolyzer measurements were performed with a methanol electrolysis cell described earlier [1]. In short, the electrolyzer cell consisted of a membrane electrode assembly (MEA), diffusion layers, polytetrafluoroethylene gaskets, graphite blocks with serpentine flow channels (Fuel Cell Technologies) and current collector plates. The membrane was a commercial Nafion® 115 (Sigma-Aldrich) proton exchange membrane (PEM) with the dimensions 2.3 cm × 2.3 cm. The electrodes were prepared by spraying catalyst onto both sides of the pre-treated membrane. The catalyst inks were prepared by mixing the catalyst (N-FWCNT for the cathode, 60 wt% Pt-Ru on carbon support (Alfa Aesar) for the anode) with isopropanol solution and Nafion ionomer (Sigma-Aldrich). The MEA was dried (vacuum 80 °C for 60 min) and weighed after painting each side to quantify the catalyst loadings as 2.1 mg $cm^{-2}$ and 1.7 mg $cm^{-2}$ for the anode and the cathode, respectively. The MEA was hot pressed at 130 °C under a pressure of 30 MPa for 120 s.

The operational electrolysis cell was stabilized overnight with a 0.4 ml $min^{-1}$ 2 M MeOH feed, 50 ml $min^{-1}$ $H_2$ purge at a temperature of 30 °C. After the stabilization MeOH feed was increased to 2 ml $min^{-1}$. Linear sweep voltammetry measurements were carried out at a rate of 1.0 mV $s^{-1}$. The stability of the cell was tested with chronoamperometry at a constant overpotential of 0.75 V for 4 weeks. The fuel feed was decreased to 0.7 ml $min^{-1}$ during that time.

### 2.2 Electrolyzer cell results

The performance of the N-FWCNT-8 catalyst was studied in a proton exchange membrane (PEM) electrolysis cell. The polarization curves for the hydrogen evolution are presented in Fig. S3a. The polarization curves reveal an onset potential for the hydrogen evolution of approximately 300 mV and an expected temperature dependent behavior; at higher temperatures mass transport and reaction kinetics are enhanced, and higher current densities are obtained. The maximum current densities achieved at the studied temperatures are 130, 180, 250, 310 and 380 mA $cm^{-2}$ for 30, 40, 50, 60 and 70 °C, respectively. The onset overpotential is higher than for the Pt/C cathode (Fig. S3b), as expected based on the half-cell polarization curves (Fig. 4). Nevertheless, when potential is increased the hydrogen production of the N-FWCNT cell increases steeper than with Pt/C. At

the straight part of the polarization curve, the cell resistance is dominated by the ohmic losses. This implies that the N-FWCNT electrode has higher ion conductivity of protons, as it is a major contributor in the ohmic losses in PEM cells [2]. Similar phenomenon has been also observed with a N-FWCNT fuel cell cathode [3].

The measured hydrogen production rate is presented in Fig. S4 together with the theoretical limit calculated from Faraday's law. The linear dependency of the $H_2$ production rate, being very close to the theoretical production rate, indicates a very high current efficiency of the electrolysis cell.

The stability of the N-FWCNT catalyst is tested by chronoamperometry at 0.75 V (Fig. S5) for one week at a time and a total of five weeks. The performance of the cell slightly decreases during the constant operation but recovers to a higher current level after cut-off indicating reversible losses resulting e.g. from mass-transfer effects. Nevertheless, the measured currents slightly reduce every period and the currents at the end of each one-week period are approximately 11.3, 10.9, 10.8, 10.0 and 9.7 mA $cm^{-2}$. Irreversible losses during the long-term measurements can include contribution from several different degradation mechanism including chemical and structural changes in the cathode and anode catalysts, the electrode layers or in the membrane. However, detailed analysis of these factors is out of the scope of this study.

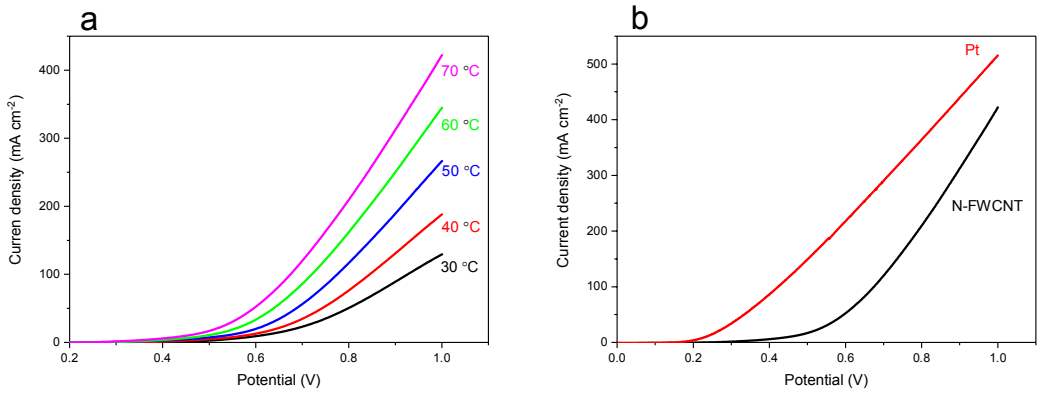


Figure S3. Polarization curves for the PEM MeOH electrolysis cell with the N-FWCNT-8 cathode at temperature range of 30 to 70 °C (a) and comparison to platinum cathode electrolyzer at 70 °C (b).

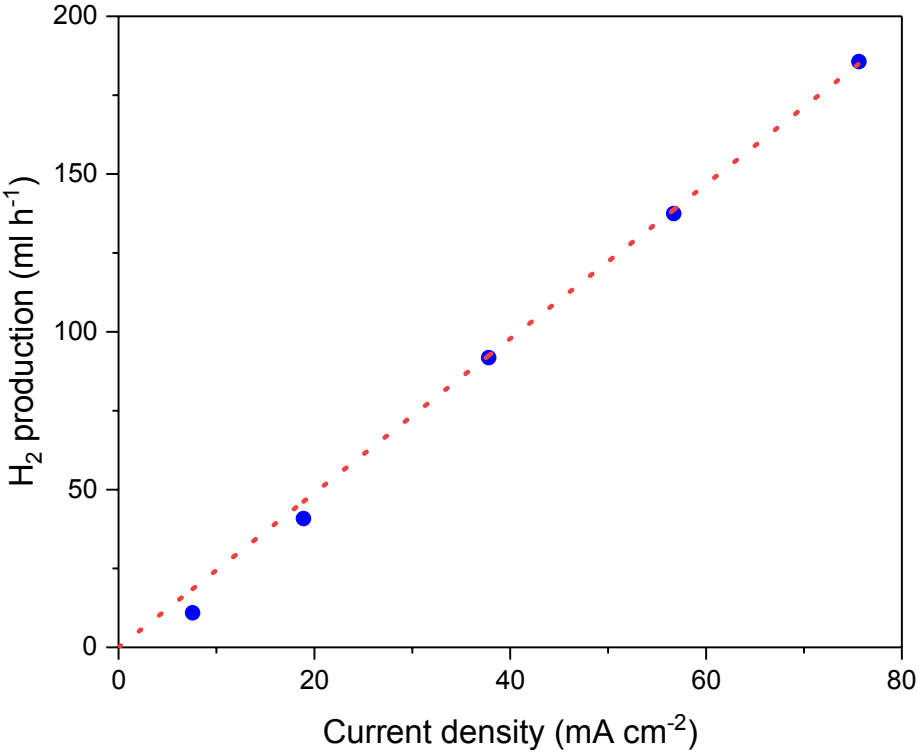


Figure S4. The hydrogen production rate as a function of current density for an electrolysis cell with the N-FWCNT-8 cathode. The circles denote experimentally obtained values, and the dotted line represents the theoretical limit.

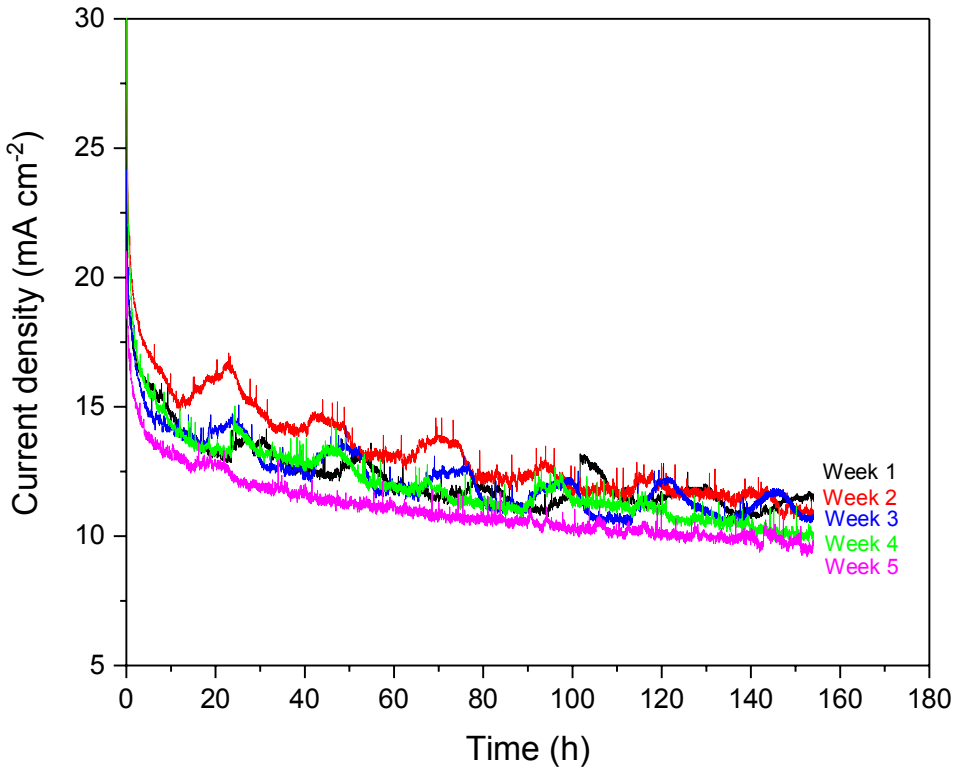


Figure S5. Constant potential electrolyzer cell measurement with N-FWCNT-8 at 0.75 V and 30 °C.

## 3 Gibbs Free Energy of Adsorption

Effectiveness of new catalytic materials are often studied with Gibbs free energy of adsorption, $\Delta G_{ads}$. This is expected to be ~ 0 eV for efficient catalysts. The approach by Nørskov et al. [4] to calculate $\Delta G_{ads}$ for different sites has been used in the study. To be able to calculate $\Delta G_{\mathrm{ads}}$, adsorption energies are first calculated as

$$\Delta E_{ads} = E_{\mathrm{N_2CNT}+n\mathrm{H}} - E_{\mathrm{N_2CNT}} - \frac{n}{2} E_{\mathrm{H_2}}, \quad \text{(S1)}$$

where $n$ is the number of adsorbing hydrogen atoms (in this study $n = 1$), $E_{\mathrm{NCNT+H}}$ is the energy of nitrogen-doped carbon nanotube with the adsorbed hydrogen, $E_{\mathrm{NCNT}}$ is the energy of nitrogen-doped carbon nanotube, and $E_{\mathrm{H_2}}$ is the energy of molecular hydrogen in the gas phase. $\Delta G_{ads}$ is defined as

$$\Delta G_{ads} = \Delta E_{ads} + \Delta E_{ZPE} - T\Delta S_{ads}, \quad \text{(S2)}$$

where $\Delta E_{\mathrm{ZPE}}$ is the change of zero-point energy during the adsorption, $T$ is the temperature (298 K), and $\Delta S_{ads}$ is the change of entropy during the adsorption. The change of zero-point energy is calculated from vibrational frequencies. The zero-point energy of all vibrational frequencies is

$$E_{ZPE} = \frac{1}{2}\sum h\nu_i, \quad \text{(S3)}$$

where $h$ is the Planck constant and $\nu_i$ corresponds to a vibrational frequency, [5] which in this case is the C-H stretching. $\Delta E_{\mathrm{ZPE}}$ is showing quite similar energies for every adsorption site. For example, there are some adsorption sites with 0.04 and 0.05 eV zero-point energy changes. For the nitrogen atoms, $\Delta E_{\mathrm{ZPE}}$ is 0.07 eV, which is slightly higher than for the carbon sites. The average of all the calculated sites is 0.05 eV. $\Delta S_{\mathrm{ads}}$ is often approximated using only the standard entropy

of molecular hydrogen as $\Delta S_{ads} = -\frac{1}{2}S^{\circ}_{H_2}$. This can be done because the contribution of vibrational entropy of adsorbed hydrogen to $\Delta S_{ads}$ is small. [6] Finally, to solve $\Delta G_{ads}$, values of $-\frac{1}{2}TS^{\circ}_{H_2} = 0.2$ eV and $E_{ZPE,H_2}$ = 0.27 eV are used [4]. Now Equation (S2) can be expressed in a simpler form as

$$\Delta G_{ads} \approx \Delta E_{ads} + 0.25 \text{ eV}. \quad \text{(S4)}$$

The calculated correction is nearly the same as the correction by Nørskov *et al.*[4], which was $\Delta G_{ads} = \Delta E_{ads} + 0.24$ eV. The calculated hydrogen adsorption energies and Gibbs free energies of adsorption can be found in the main text.

## 4 Coordinates of the reactions presented in Figures 9 and 10.

Figure S6 show the Initial, Transition and Final States (IS, TS and FS) of the Volmer reaction C1-C5C9. All the coordinates of the IS, TS and FS of all the NEB paths shown in Figures. 9 and 10 are included to the SI. The naming of the files is following: The reaction, state (IS,TS,FS), charge, occupation. An example: Volmer-e-TS-q-1-C1-C5C9.xyz which means a Volmer reaction, Transition State, charge q=-1, hydrogen approaching to site C1 while site sites C5 and C9 are occupied. In neutral systems the charge has not been noted.

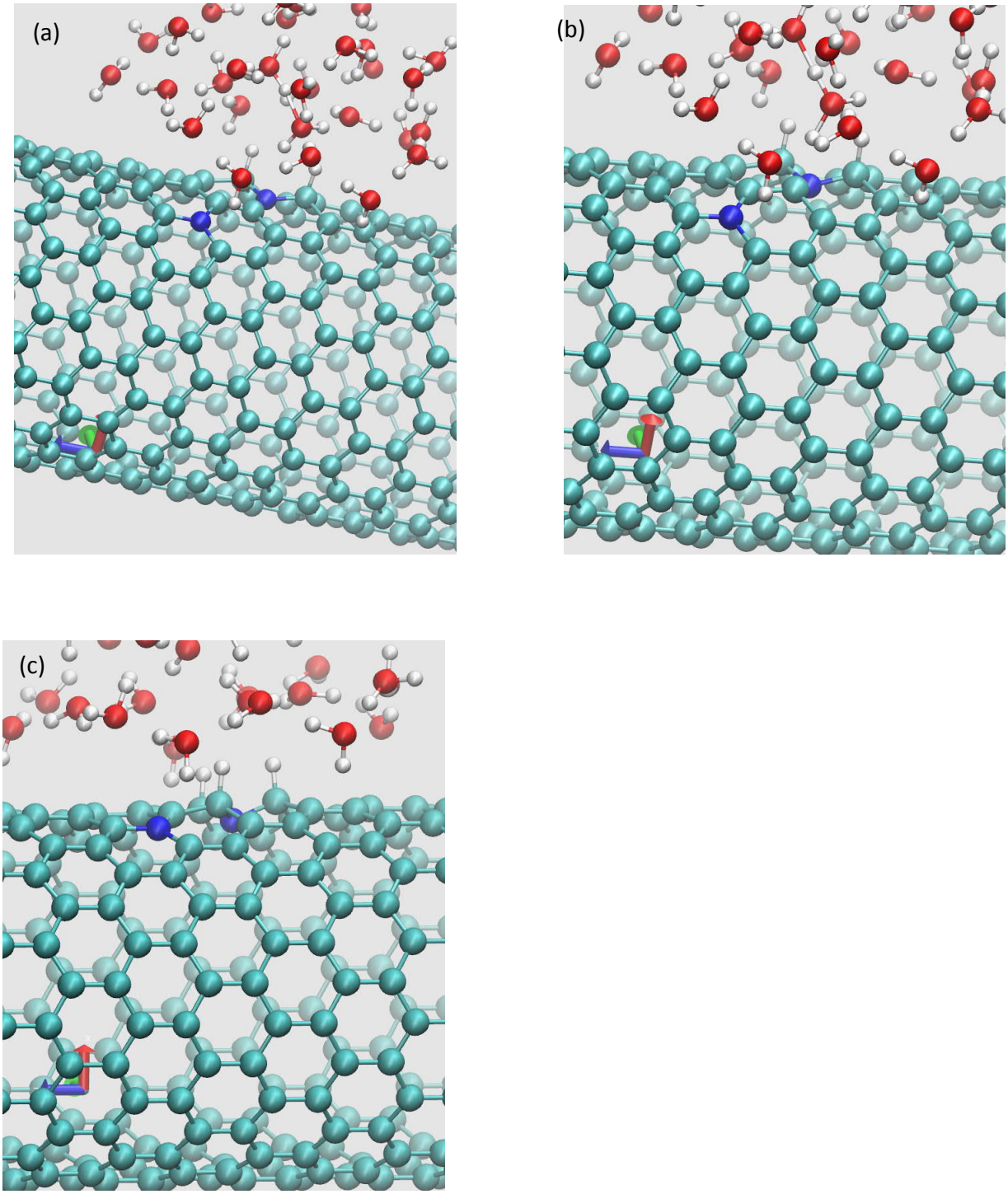


Figure S6. Initial (a), Transition (b) and Final State (c) of the Volmer reaction. The hydrogen approach to the site C1 and the sites C5 and C9 are occupied.

## 5 Validation of the Water Cluster Model

There is no unequivocal way to treat water and hence to select initial configurations for reactions. For example, Das et al. [7] used a model of protonated water (four water molecules) by Hodges and Wales [8]. Previously our research group published a paper on the HER on CNTs with a molecular dynamics simulation for a structure of 331 water molecules with CNT and selected a snapshot, which was then used for the NEB calculations [6]. Even though these two studies used different approach to study the reaction barriers of the HER, these are in good agreement with each other.

The validation of the used water cluster model of 33 water molecules has been done on the pristine and nitrogen-doped (14,0) CNTs and the results are compared with two different studies. Example of the system is shown in Fig. S6. The Heyrovský reaction was used in the validation. The validation was started with the pristine CNT with two different initial distance between the adsorbed and reactive protons (Fig. S7). The shorted distance (1.91 Å) produce notably lower reaction barrier and the longest distance (2.30 Å) produced a reaction barrier which is in a good agreement with other studies (Table S2). When the distance *d* have been found for the pristine CNT, the whole system is reoptimized and the water structure with the nitrogen-doped CNT is validated. In further studies, initial conditions were selected so that the distance between the adsorbed and reactive protons was approximately 2.30 Å.

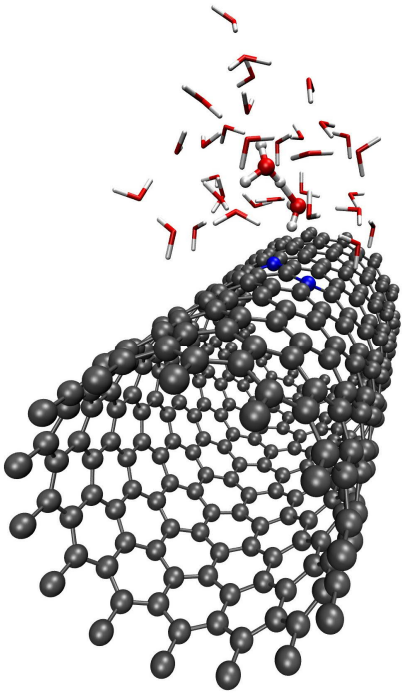

Figure S7. An initial condition for the first Volmer reaction. The active Zundel cation is shown in the ball-and-stick representation. The water molecules with the stick representation were kept at the fixed positions.

Table S2. Calculated reaction barriers of the Heyrovský reaction on pristine and nitrogen-doped CNTs.

| | Reaction barrier (eV) | Endo-/exothermic | Reference |
|---|---|---|---|
| (14,0) CNT | 0.97 | Exothermic | This work |
| (14,0) CNT | 1.09 | Endothermic | [6] |
| (10,10) CNT | 1.04 | Exothermic | [7] |
| (14,0) NCNT | 1.29 | Exothermic | This work |
| (14,0) NCNT | 1.33 | Endothermic | [6] |

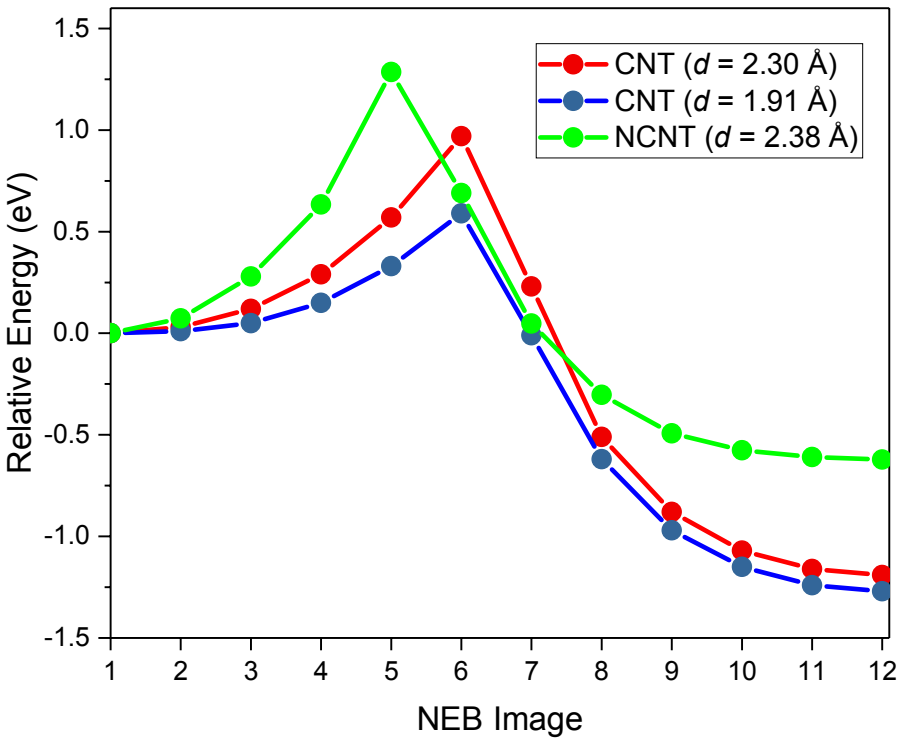


Figure S8. The reaction barriers of the Heyrovský reaction. The initial distance, *d*, between the reactive proton and adsorbed proton is also shown.

## 6 Brønsted-Evans-Polanyi Relationship

The Brønsted-Evans-Polanyi (BEP) relationship is shown in Fig. S8, which reveals that the linear relationship of the reaction barriers and adsorption energies is not very good. However, the BEP relationship show the increasing and decreasing trend for the Volmer and Heyrovský reactions, respectively, as observed before. [6]

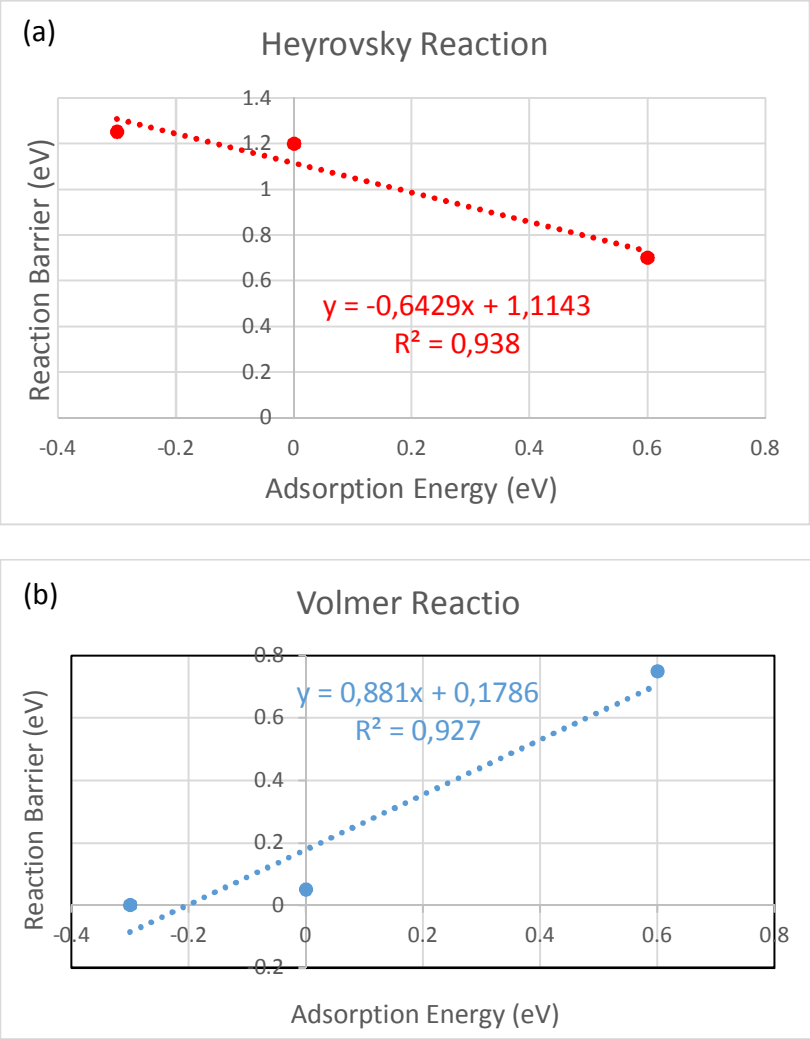


Figure S9. The Brønsted-Evans-Polanyi relationship for the Heyrovský (a) and Volmer (b) reactions.

## 7 References


1. Tuomi, S., Guil-Lopez, R., & Kallio, T., *J. Catal.*, 334 (2016) 102-109.

2. O'Hayre, R., Cha, S., Colella, W., & Prinz, F. B., *Fuel cell fundamentals*, John Wiley & Sons, Inc, 2016, 117-166.

3. Kanninen, P., Borghei, M., Sorsa, O., Pohjalainen, E., Kauppinen, E. I., Ruiz, V., & Kallio, T. *Applied Catalysis B: Environmental*, 221 (2014) 341-349.

4. Nørskov, J. K., Bligaard, T., Logadottir, A., Kitchin, J. R., Chen, J. G., Pandelov, S., & Stimming, U., *J. Electrochem. Soc.*, 152 (2005) J26.

5. Zheng, Y., Jiao, Y., Jaroniec, M., & Qiao, S. Z., *Angewandte Chemie International Edition*, 54 (2015) 52-65.

6. Holmberg, N., & Laasonen, K., *J. Phys. Chem. C*, 119 (2015) 16166-16178.

7. Das, R. K., Wang, Y., Vasilyeva, S. V., Donoghue, E., Pucher, I., Kamenov, G., Cheng, H., & Rinzler, A. G., *ACS Nano,* 8 (2014) 8447-8456.

8. Hodges, M. P., & Wales, D. J., *Chem. Phys. Lett.*, 324 (2000) 279-288